ADVANCED FUNCTIONAL MATERIALS

Supporting Information

for *Adv. Funct. Mater.*, DOI 10.1002/adfm.202415735

Electronic Coupling Between Perovskite Nanocrystal and Fullerene Modulates Hot Carrier Capture

Yusheng Li, Junke Jiang, Dandan Wang, Dong Liu, Shota Yajima, Hua Li, Akihito Fuchimoto, Hongshi Li, Guozheng Shi, Shuzi Hayase, Shuxia Tao, Jiangjian Shi, Qingbo Meng*, Chao Ding* and Qing Shen**

Supporting Information

Electronic Coupling Between Perovskite Nanocrystal and Fullerene Modulates Hot Carrier Capture

Yusheng Li[a]†, Junke Jiang[b,e]†, Dandan Wang[a]†, Dong Liu[a], Shota Yajima[a], Hua Li[a], Akihito Fuchimoto[a], Hongshi Li[c], Guozheng Shi[a], Shuzi Hayase[a], Shuxia Tao*[b], Jiangjian Shi[d], Qingbo Meng*[d], Chao Ding*[a,f], Qing Shen*[a]

[a.] Faculty of Informatics and Engineering, The University of Electro-Communications, 1-5-1 Chofugaoka, Chofu, Tokyo 182-8585, Japan.

[b.] Materials Simulation and Modelling, Department of Applied Physics, Eindhoven University of Technology, 5600 MB Eindhoven, The Netherlands.

[c.] Institute of New Energy Materials Chemistry, School of Materials Science and Engineering, Nankai University, TongYan street 38, Jinnan District, Tianjin 300350, China

[d.] Key Laboratory for Renewable Energy, Beijing Key Laboratory for New Energy Materials and Devices, Chinese Academy of Sciences, Beijing 100190, P. R. China

[e.] Present Address: Univ Rennes, INSA Rennes, CNRS, Institut FOTON - UMR 6082, F-35000 Rennes, France

[f.] Present Address: Institute of New Energy and Low-Carbon Technology, Sichuan University, Chengdu 610065, P. R. China

† These authors contributed equally

*Corresponding authors: S.X.Tao@Tue.nl; qbmeng@iphy.ac.cn; ding@jupiter.pc.uec.ac.jp; shen@pc.uec.ac.jp

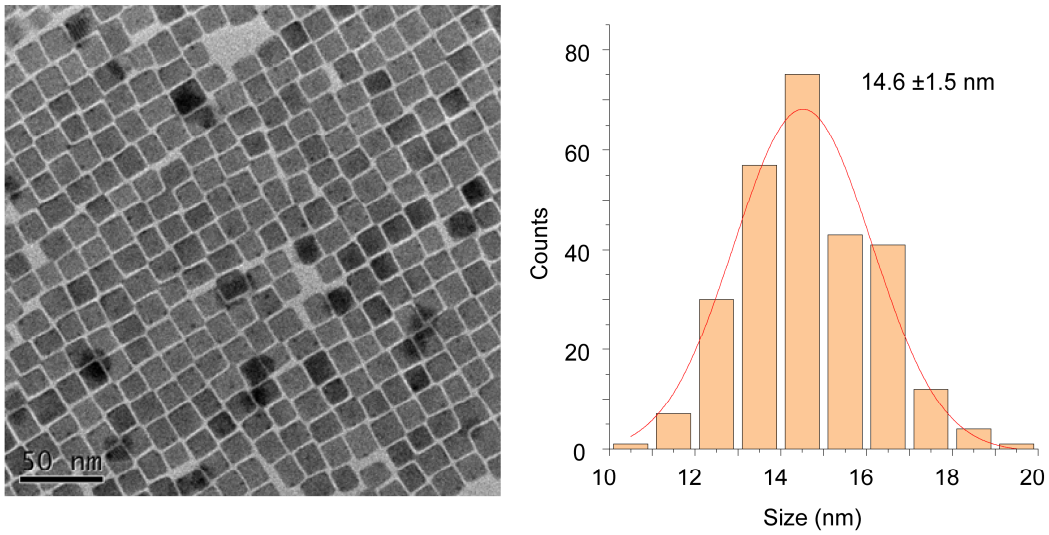

Figure S1. Transmission electron microscopy image of synthesized $CsPbI_3$ nanocrystals (NCs) and their size distribution statistics. The average diameter of the as-prepared $CsPbI_3$ NCs is approximately 14.6 nm.

Supplementary Note 1: Density Functional Theory (DFT) Calculation Details and Supplementary Results

Figures S2-S4 and Table S1 present the results of DFT calculations, including structural models, binding configurations, calculated ligand binding affinities, charge density differences, bond length and bond order analysis. In exploring the interaction of [6,6]-phenyl-C61-butyric acid (PCBA) with the $CsPbI_3$ surface, both its carboxylate (PCBA-COO^-) and carboxylic acid (PCBA-COOH) forms were considered. However, experimental evidence indicates that PCBA primarily interacts with the NC surface in its PCBA-COO^- form (Figure S12). Computational models (Figure S3) further show that while PCBA-COOH exhibits stronger binding energy than [6,6]-phenyl-C61-butyric acid methyl ester (PCBM), it binds less strongly than PCBA-COO^- to the $CsPbI_3$ surface. This suggests that even if some PCBA remains in its non-ionized COOH form, PCBA-COO^- is the dominant contributor to the strong binding observed. Therefore, for simplicity, we refer to PCBA throughout the main text and subsequent

sections in its carboxylate form. The strength and type of interactions between the ligands and the perovskite surface were evaluated using ligand binding affinity (E_b) and bond order. E_b reflects the overall strength of the ligand-surface interaction, while bond order correlates with the electron density at bond-critical points (saddle points of electron density along bond paths), where a higher bond order indicates a stronger covalent bond. These results are shown in Figure S3 and Table S1. For PCBA and $CsPbI_3$ NC, the chemical bonding through terminal functional groups with surface atoms of the perovskite is shown to be more stable than the physical contact configuration of C_{60} with the NC surface. This is evidenced by the larger negative binding energy values (approximately -4 eV) as well as the higher bond order of Pb-O and Cs-O for PCBA, regardless of surface termination, illustrating that PCBA can spontaneously anchor onto the NC surface similarly to OA. In contrast, the small binding energy (almost zero for two configurations) between PCBM and $CsPbI_3$ NCs demonstrates a weak interaction. Figure S4 shows the charge density difference (CDD) analysis. PCBM exhibits no significant charge redistribution at the interface, further suggesting weak physical adsorption on the perovskite surface. In contrast, the significant charge redistribution observed for PCBA suggests chemical bonding formation with the perovskite surface.

Furthermore, the detailed chemical bonding mode of $CsPbI_3$ NC-PCBA was investigated through bond length and bond order analysis and compared with $CsPbI_3$ NC-OA (Table S1). Similar to OA, PCBA binds to both CsI- and PbI_2-terminated slabs via covalent bonds. On PbI_2-terminated NCs, both Pb-O bond lengths ($L_{Pb\text{-}O(1)} \approx 2.51$ Å and $L_{Pb\text{-}O(2)} \approx 2.43$ Å) are smaller than the sum of Pb^{2+} (1.2 Å) and O^{2-} (1.4 Å) ion radii, and the bond orders are larger than 0.3, illustrating that effective bonding is realized by bidentate chelating between the two O atoms of PCBA and Pb atoms. Unlike PbI_2-termination, the bonding in CsI-termination is realized with a bidentate bridging

mode, where two O atoms bond with Pb and Cs atoms separately, evidenced by bond order of 0.42 and 0.16. Whether the bonding mode is bidentate bridging or chelating, such bonding through multiple atoms has been shown to provide extra stability to the complex for coupling than physical absorption within $CsPbI_3$ and PCBM.

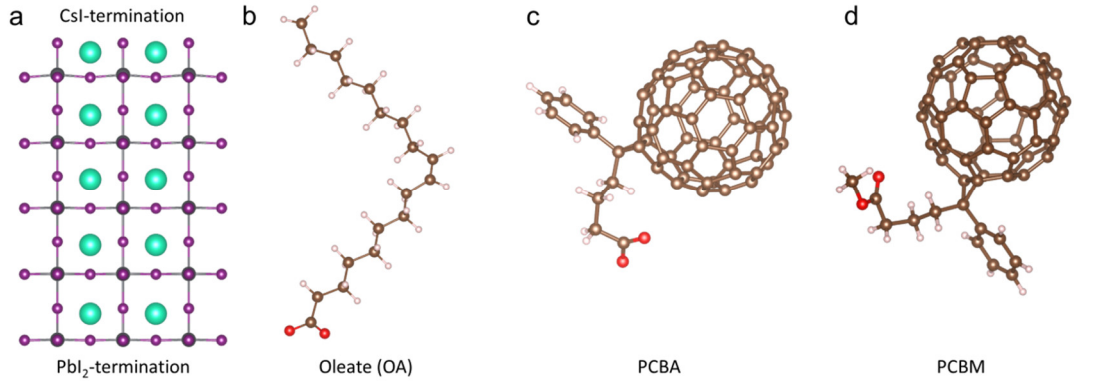

Figure S2. (a) Structural models of $CsPbI_3$ with CsI-termination on the top and PbI_2-termination on the bottom. Molecular structure of (b) oleate ($C_{18}H_{34}O_2^-$: OA^-), (c) PCBA, and (d) PCBM, respectively.

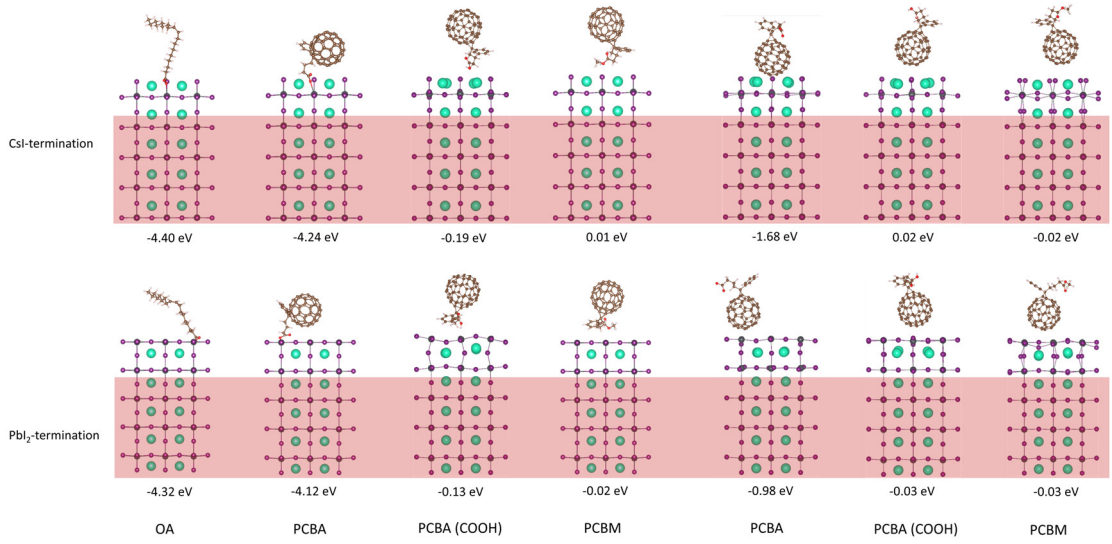

Figure S3. Binding configurations and calculated ligand binding affinity of $CsPbI_3$ surfaces passivated by OA, PCBA (carboxylate), PCBA-COOH (carboxylic acid), and PCBM ligands. The calculations consider both CsI-terminated and PbI_2-terminated perovskite surfaces, as well as different relaxed configurations for PCBA, PCBA-

COOH, and PCBM. During geometry optimization, the layers within the red rectangles were fixed, while the top layers, including the ligands, were relaxed.

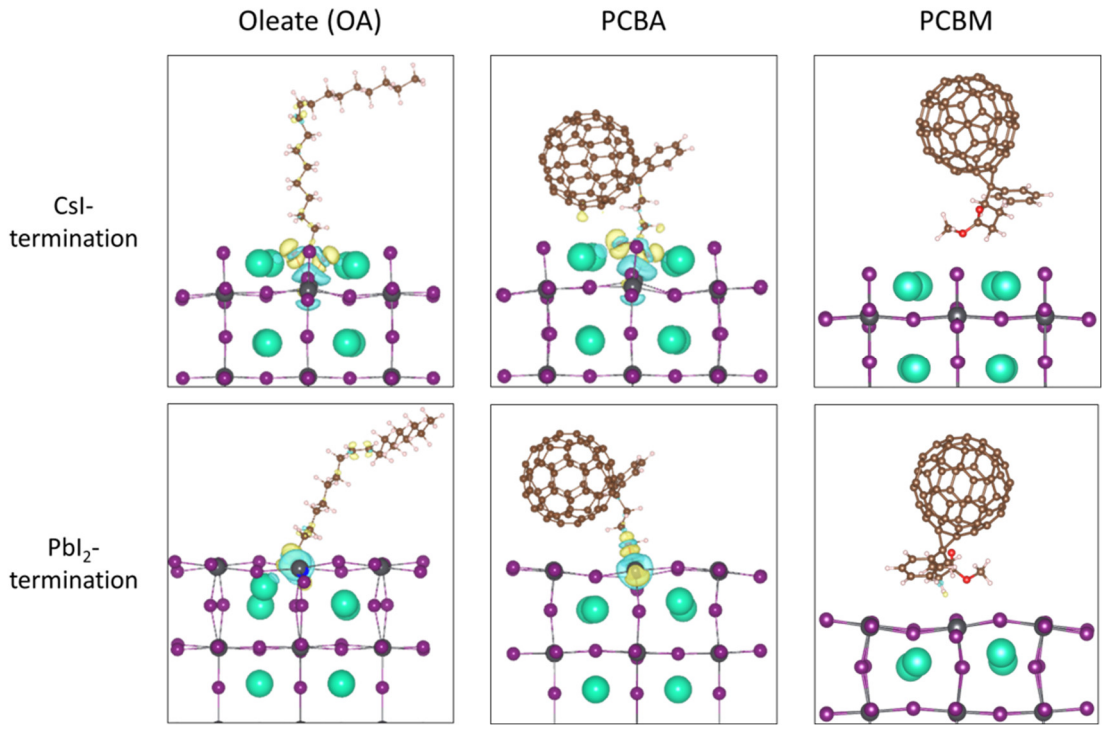

Figure S4. The charge density difference of $CsPbI_3$-PCBA, and $CsPbI_3$-PCBM with CsI-termination and PbI_2-termination, respectively. The yellow and cyan regions indicate the charge accumulation and depletion, respectively, and the isosurface is 0.002 e/Å^3.

Table S1. Bond lengths and bond order of two oxygens with nearest Pb, C and Cs atoms.

		Pb-O (1)	Pb-O (2)	C-O (1)	C-O (2)	Cs-O (1)	Cs-O (2)
CsI-termination OA	Distance (Å)	2.83	2.46	1.26	1.30	3.13	3.14
	Bond order	0.17	0.36	1.60	1.46	0.12	0.12

CsI-termination PCBA	Distance (Å)	3.21	2.42	1.26	1.30	2.98	3.16
	Bond order	0.07	0.42	1.64	1.44	0.16	0.10
CsI-termination PCBA-COOH	Distance (Å)	-	-	1.22	1.38	3.36	-
	Bond order	-	-	1.80	1.14	0.10	-
CsI-termination PCBM	Distance (Å)	-	-	1.22	1.36	5.08	4.09 (I-O)
	Bond order	-	-	1.78	1.13	0.002	0.03 (I-O)
PbI_2-termination OA	Distance (Å)	2.44	2.44	1.28	1.28	3.20	3.20
	Bond order	0.42	0.40	1.50	1.52	0.09	0.08
PbI_2-termination PCBA	Distance (Å)	2.51	2.43	1.27	1.29	-	-
	Bond order	0.31	0.37	1.53	1.47	-	-
PbI_2-termination PCBA-COOH	Distance (Å)	4.53	-	1.21	1.37	-	3.62 (I-O)
	Bond order	0.006	-	1.79	1.19	-	0.05 (I-O)
	Distance (Å)	4.43	5.22	1.22	1.36	-	-

PbI_2-termination PCBM	Bond order	0.005	0.001	1.78	1.13	-	-

The ion radii of Pb^{2+}, Cs^{+} and O^{2-} are 1.2 Å, 1.67 Å and 1.4 Å respectively. Bonding modes (bidentate mode, bridging mode and monodentate mode) are distinguished by comparing the bond length with the sum of related atom radii.

Supplementary Details on the $CsPbI_3$ NC-fullerene Hybrids

Figures S5-8 provide supplementary details on the $CsPbI_3$ NC-fullerene hybrid systems mentioned in the main manuscript, including fullerene molecular structures, molecular synthesis verification via nuclear magnetic resonance (NMR) spectroscopy, crystal structure information of $CsPbI_3$ NCs and $CsPbI_3$ NC-fullerene hybrids as shown by X-ray diffraction (XRD) patterns, and the optical properties of these hybrids as demonstrated by absorption spectra.

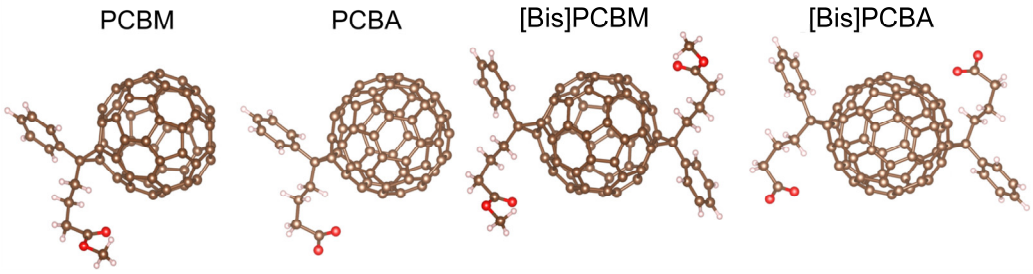

Figure S5. Molecular structures of PCBM, PCBA, Bis(1-[3-(methoxycarbonyl) propyl]-1-phenyl)-[6.6]C62 ([Bis]PCBM), and [Bis]PCBA. We note both [Bis]PCBM and [Bis]PCBA are the mixture of isomers. Here, we only show one structure of the isomers.

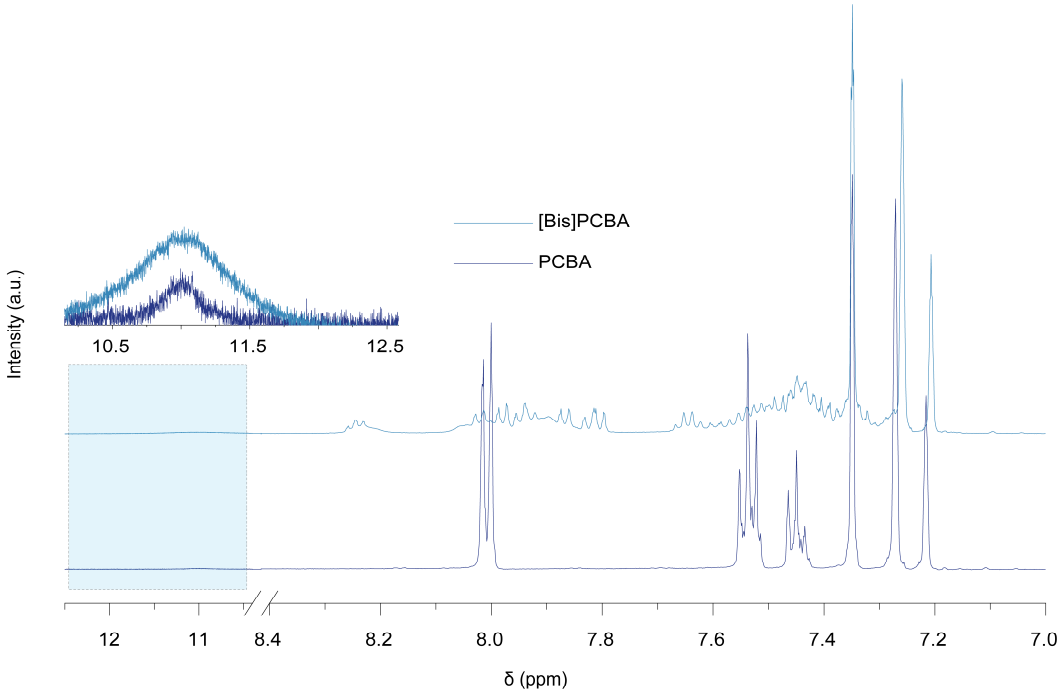

Figure S6. NMR spectroscopy of PCBA and [Bis]PCBA. The inset zooms in on the chemical shift region for the hydrogen atom in the -COOH group.

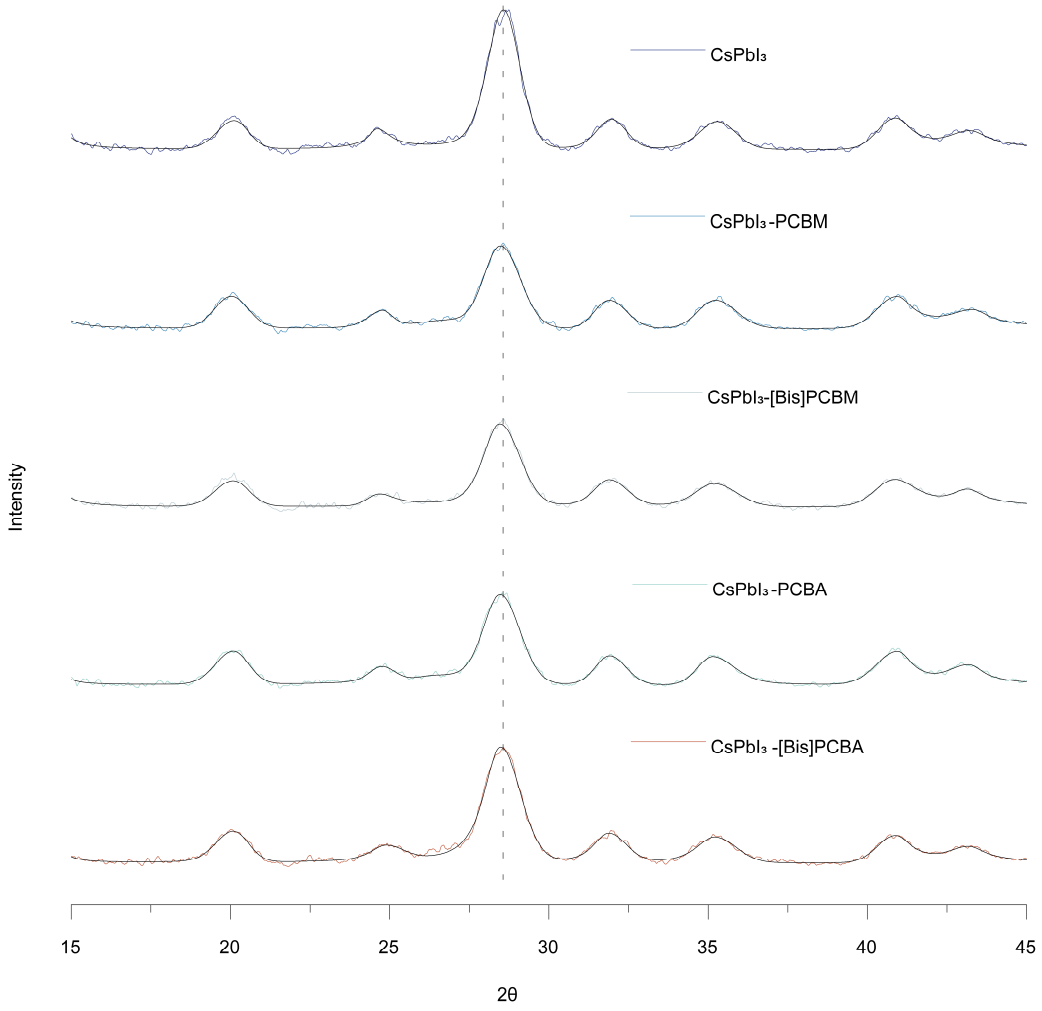

Figure S7. Powder XRD patterns of $CsPbI_3$ NCs and $CsPbI_3$ NC-fullerene hybrids. All samples display as identical cubic phase.

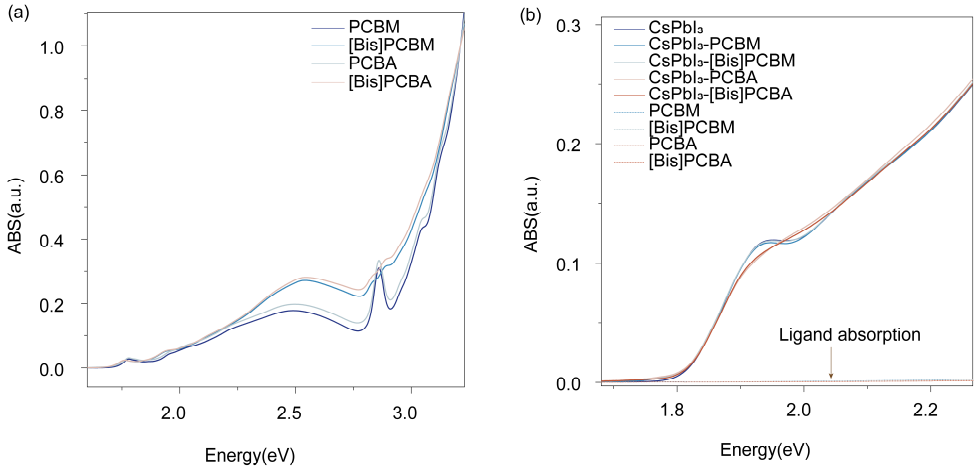

Figure S8. (a) Absorption spectra of PCBM, PCBA, [Bis]PCBM, and [Bis]PCBA. (b) Absorption spectra of colloidal $CsPbI_3$ NCs, $CsPbI_3$ NC-fullerene hybrid dispersions,

and pure fullerene molecular solution. Compared to the intrinsic absorption of $CsPbI_3$ NCs, the absorption contribution from fullerene is negligible.

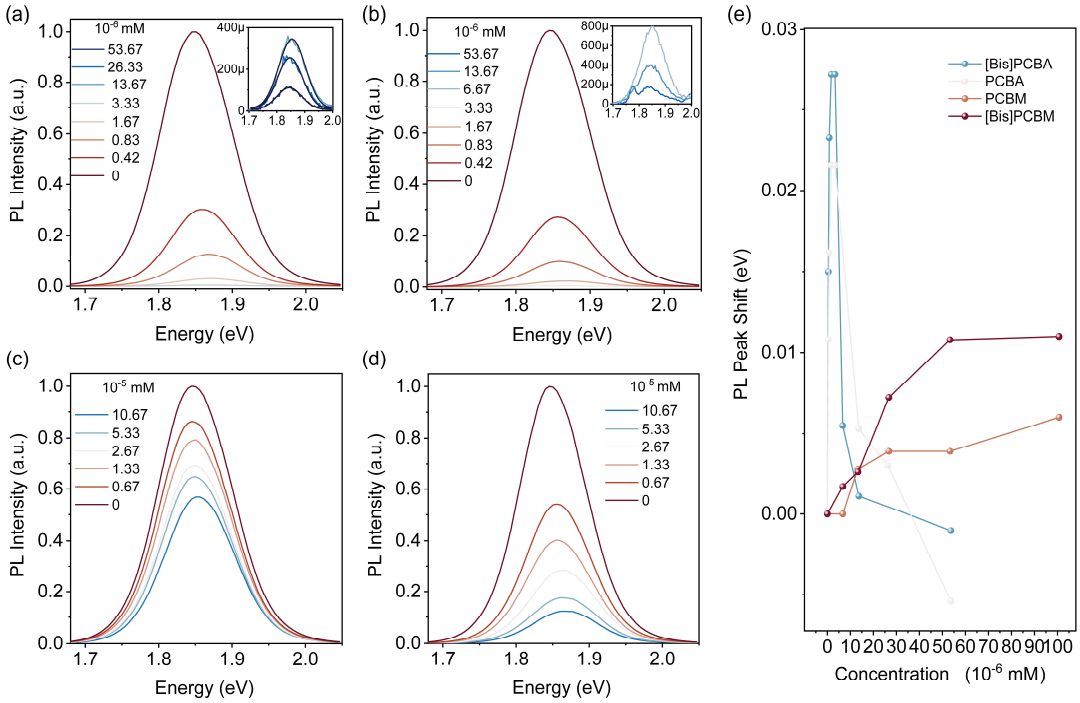

Figure S9. Photoluminescence (PL) spectra of $CsPbI_3$ NCs colloidal solution titrated with varying quantities of (a) PCBA, (b) [Bis]PCBA, (c) PCBM, and (d) [Bis]PCBM. (e) Shift of PL maxima relative to the PL maxima of intrinsic $CsPbI_3$ NCs. Note that the abnormal PL signal at 5.367×10^{-6} mM [Bis]PCBA (inset of (b)) is due to scattered light from the environment. The shift in the peak positions in panel (e) is consistent with the stage characteristics of the Stern−Volmer plots. The observed spectral shifts are likely caused by the combined effects of exciton delocalization and charge transfer states, which are predominantly influenced by the varying interactions between $CsPbI_3$ NCs and different fullerene derivatives.

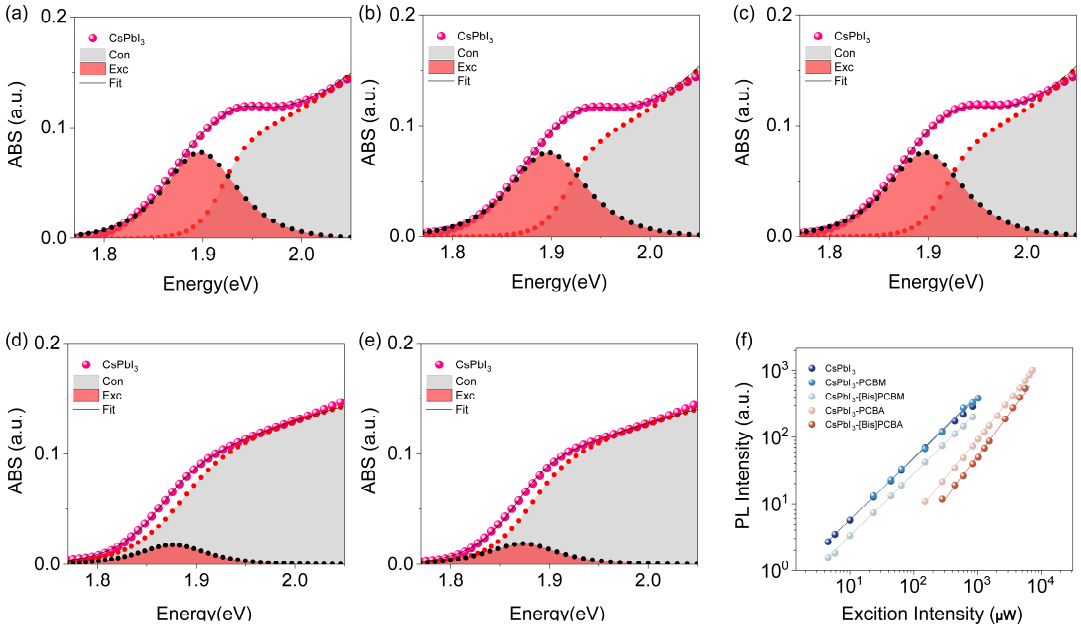

Figure S10. (a-e) Band edge absorption spectra of $CsPbI_3$ NC, $CsPbI_3$ NC-PCBM, $CsPbI_3$ NC-[Bis]PCBM, $CsPbI_3$ NC-PCBA, and $CsPbI_3$ NC-[Bis]PCBA, fitted with the Elliott formula.[1] The black lines represent the fitting results, incorporating contributions from continuous band (Con) and exciton absorption (Exc). The exciton binding energies (E_b) are 25 meV for $CsPbI_3$ NC, $CsPbI_3$ NC-PCBM, and $CsPbI_3$ NC-[Bis]PCBM, and 7 meV for $CsPbI_3$ NC-PCBA and $CsPbI_3$ NC-[Bis]PCBA, respectively. The reduced E_b values for $CsPbI_3$ NC-PCBA and $CsPbI_3$ NC-[Bis]PCBA suggest efficient exciton dissociation due to the formation of stable donor-acceptor complexes. (f) Excitation power-dependent PL spectra. The PL intensity (I_{PL}) was fitted to the excitation laser power (L_{exc}) using the power law $I_{PL} \sim L_{exc}^{\alpha}$, where the laser wavelength was 470 nm. The coefficients α were approximately 0.98 for $CsPbI_3$ NC, $CsPbI_3$ NC-PCBM, and $CsPbI_3$ NC-[Bis]PCBM, indicating bound exciton emission. For $CsPbI_3$ NC-PCBA and $CsPbI_3$ NC-[Bis]PCBA, α values were about 1.42, indicating exciton delocalization. This suggests that the energy level alignment at the interface creates a local electric field, lowering the potential barrier at the quantum boundaries.

Supplementary Note 2: Stern-Volmer Quenching Models Used in the Manuscript

Figures 2a-c in the main text describe different systems at various stages, which involve complex interactions characterized by multiple quenching modes, including dynamic quenching, static quenching, and combined dynamic and static quenching. While some of these modes derive directly from standard quenching paradigms, others represent deviations tailored to the specific characteristics of our systems. This note elaborates

on the standard dynamic and static quenching models and details the specific models applied in Figures 2a-c.

Standard Dynamic Quenching

In the dynamic quenching mechanism, fluorophores and quenchers are independently dispersed in the solution prior to photoexcitation. Upon excitation, a fluorophore transitions from its ground state [F] to its excited state [F*]. Before [F*] can relax back to [F] spontaneously, it may collide with a quencher molecule [Q]. This collision facilitates the non-radiative release of the excited-state energy, returning the fluorophore to its ground state without any permanent chemical changes to either molecule. This process is purely photophysical or may involve the formation of transient exciplexes. Importantly, dynamic quenching affects only the excited-state properties of the fluorophore, leaving the ground-state absorption spectrum of [F] unchanged. The process can be described by the equilibrium:

$$F* + Q \rightarrow F + Q*$$

Under steady-state photoluminescence (PL) conditions, dynamic quenching reaches equilibrium under continuous illumination. In the absence of a quencher, the rate equation is given by:

$$\frac{d[F^*]}{dt} = G(t) - \gamma[F*]_0 = 0$$

In the presence of a quencher, the rate equation becomes:

$$\frac{d[F^*]}{dt} = G(t) - \gamma[F*] - \kappa[F*][Q] = 0$$

Here, [F*] and [F*]$_0$ represent the concentrations of the excited fluorophore in the presence and absence of the quencher, respectively. [Q] is the quencher concentration, $G(t)$ is the generation rate of [F*] under continuous illumination, γ is the intrinsic recombination rate, and κ is the collision rate constant. Solving these equations yields the relationship between the excited-state concentrations:

$$\frac{[F^*]_0}{[F^*]} = 1 + \left(\frac{\kappa}{\gamma}\right)[Q] = 1 + K_D[Q]$$

Since the PL intensity is proportional to the concentration of the excited fluorophore, the Stern-Volmer equation for dynamic quenching is expressed as:

$$F_0/F = 1 + K_D[Q]$$

where F_0 and F are the PL intensities in the absence and presence of the quencher, respectively, and K_D is the dynamic quenching constant.

Standard Static Quenching

Static quenching involves the formation of a non-fluorescent ground-state complex [$F{\cdot}Q$] through chemical bonding between the fluorophore and quencher. Unlike dynamic quenching, energy transfer in static quenching occurs without collisional encounters and is typically faster. The formation of this complex often leads to observable changes in the absorption spectrum due to the altered electronic environment. The process can be described by the equilibrium:

$$[F] + [Q] \rightarrow [F \cdot Q]$$

The static quenching constant K_s is defined as

$$K_s = \frac{[F \cdot Q]}{[F][Q]} = \frac{[F_0] - [F]}{[F][Q]}$$

By relating the concentrations to PL intensities and rearranging, the Stern-Volmer equation for static quenching becomes:

$$F_0/F = 1 + K_s[Q]$$

Downward Deviation from the Stern-Volmer Equation (Applicable to Figure 2b)

In this scenario, the total fluorophore population [F_0] comprises both inaccessible [F_{i0}] and accessible [F_{a0}] fluorophores:

$$[F_0] = [F_{i0}] + [F_{a0}]$$

Only the accessible fluorophores contribute to quenching, adhering to the standard dynamic quenching model. The PL intensities can thus be expressed as:

$$F_0 = F_{i0} + F_{a0}$$

$$F = \frac{F_{a0}}{(1 + K_a[Q])} + F_{i0}$$

Subtracting these equations and rearranging leads to:

$$F_0/\Delta F = 1/f_a K_a Q + 1/f_a$$

where $\Delta F = F_0 - F$, $f_a = F_{a0}/F_0$ is the fraction of initial PL from accessible fluorophores, and K_a is the quenching constant for the accessible population. This formulation represents a simple linear relationship between $F_0/\Delta F$ and $1/[Q]$, which simplifies the representation while providing a clearer and more reliable framework for determination of the fraction of accessible fluorophores (f_a) and the quenching constant (K_a) through linear regression.

Combined Dynamic and Modified Static Quenching (Applicable to the first stage of the Stern-Volmer plots in Figure 2c)

To accurately depict the positive curvature, we have developed a formula that combines the standard dynamic quenching model with a modified static quenching model. This approach is particularly relevant for our NC systems where the NC possesses multiple binding sites for the fullerene molecules. Our starting point is the general equation that describes the combined effects of dynamic and static quenching:

$$\frac{F_0}{F} = (K_d[Q] + 1)(K_s[Q] + 1)$$

In this equation, K_d represents the dynamic quenching constant, K_s represents the static quenching constant, and $[Q]$ denotes the quencher concentration. This equation assumes a straightforward 1:1 ground-state complex formation between the fluorophore and the quencher.

Recognizing that NCs have a large surface area, we considered that the number of quenchers binding to a single NC may exceed one. Consequently, we modified the binding constant K_b for the static complex to account for multiple binding sites. The reaction can be represented as:

$$[F] + n[Q] \rightarrow [F \cdot nQ]$$

where n is the number of binding sites per NC. Therefore, the binding constant K_b for the static complex can be expressed as:

$$K_b = \frac{[F \cdot nQ]}{[F][Q]^n} = \frac{[F_0] - [F]}{[F][Q]^n}$$

This modification leads to a new static quenching equation:

$$\frac{F_0}{F} = (K_b[Q]^n + 1)$$

To integrate both dynamic and static quenching mechanisms, we proposed that the fraction of fluorescence intensity not quenched by collision (f_d) and not complexed (f_s) can be described as:

$$\frac{F}{F_0} = f_d \cdot f_s$$

Thus, the overall quenching equation that includes both dynamic and static quenching for systems with multiple binding sites is:

$$F/F_0 = [1/(K_d[Q] + 1)][\frac{1}{(K_b[Q]^n + 1)}]$$

The quenching equation can be written as

$$F_0/F = [(K_d[Q] + 1)][(K_b[Q]^n + 1)]$$

Standard Dynamic Quenching with Baseline Shift (Applicable to the second stage of the Stern-Volmer plots in Figure 2c)

As the quencher concentration $[Q]$ increases, the static quenching sites on the NCs become fully occupied, leading to the formation of NC-fullerene complexes. At this stage, the remaining quenching primarily proceeds through dynamic interactions between the formed complexes (or any unquenched fluorophores) and the free quenchers. However, due to the saturation of the static quenching sites, the fluorescence intensity no longer returns to the original baseline, but rather shows a shift upward. To account for this baseline shift, we modify the standard dynamic quenching equation.

Initially, when both dynamic and static quenching are active, the quenching behavior can be described by the combined equation:

$$F_0/F = [(K_{d1}[Q] + 1)][(K_b[Q]^n + 1)]$$

Here, K_{d1} represents the quenching constant between the formed complexes (or any unquenched fluorophores) and the free quenchers in the second stage. As the quencher concentration $[Q]$ increases further, the static sites become fully occupied, which can be approximated by the condition $K_B[Q]^n \gg 1$, leading to:

$$K_b[Q]^n + 1 \approx K_b[Q]^n$$

After this saturation, the effective fluorescence intensity is primarily governed by dynamic quenching interactions between the formed complexes (or any unquenched fluorophores) and the free quenchers. The fluorescence intensity at this stage can be expressed as:

$$F = \frac{F_0}{(1 + K_{d1}[Q])K_b[Q]^n}$$

Given that $K_b[Q]^n$ has become very large, we can treat it as a constant b, representing the baseline shift due to the saturation of static quenching sites:

$$b = K_b[Q]_{sat}^n$$

where $[Q]_{sat}$ is the concentration of quencher at which the static sites become fully saturated. Substituting b into the expression for fluorescence intensity, we now have:

$$F = \frac{F_0}{b(1 + K_{d1}[Q])}$$

Rearranging this equation yields:

$$\frac{F_0}{F} = b(1 + K_{d1}[Q])$$

To further simplify, we introduce a new dynamic quenching constant for the second stage, denoted as $K_{d2}=bK_{d1}$. Thus, the final modified Stern-Volmer equation becomes:

$$F_0/F = b + K_{d2}[Q]$$

Table S2. Parameters fitted from Stern−Volmer plots

	K_a (M^{-1})	f_a	K_d (M^{-1})	n	K_b (M^{-n})	K_{d2} (M^{-1})
PCBM	5.71×10^7	48.9%				
[Bis]PCBM	1.46×10^8	92.0%				
PCBA			2.47×10^6	2.06	2.09×10^{12}	8.52×10^7
[Bis]PCBA			1.21×10^7	2.12	1.84×10^{13}	2.22×10^8

Supplementary Note 3: Discussion on the Preferential Anchoring Modes of Fullerene Molecules onto $CsPbI_3$ NCs

We performed X-ray photoelectron spectroscopy (XPS) analysis to investigate the bonding interactions (Figure S11). For samples prepared by directly dipping NC colloidal solutions onto quartz glass, we found that the peaks of Pb 4f, Cs 3d, and I 3d remained nearly unchanged after the introduction of fullerene. However, when we spin-coated the fullerene onto a $CsPbI_3$ NC film with alkyl ligands removed using methyl acetate, we observed visible shifts in binding energy compared to the intrinsic $CsPbI_3$ NCs (with removed ligands). Specifically, PCBA and [Bis]PCBA caused the Pb 4f core level to shift towards higher energies and the Cs 3d/5 and I 3d levels towards lower binding energies compared to PCBM and [Bis]PCBM. These shifts in binding energy led us to speculate that the interaction strength order is OA≥PCBA/[Bis]PCBA>>PCBM/[Bis]PCBM. This suggests that PCBA and [Bis]PCBA preferentially anchor onto atoms not capped with OA rather than extensively replacing the OA group through traditional ligand exchange. These results are consistent with the predictions from DFT calculations.

For attenuated total reflection Fourier transform infrared spectroscopy (ATR-FTIR) measurements, we firstly prepared solid film samples on silicon substrates using the same methods as the first group of XPS but with an excessive addition of fullerene. As shown in Figure S12 (a), oleic acid (OA), PCBM, and PCBA exhibit distinguishable characteristic stretching vibrations of the carbonyl group: υ_{OA}(C=O) ≈ 1708 cm^{-1}, υ_{PCBM}(C=O) ≈ 1708 cm^{-1}, and υ_{PCBA}(C=O) ≈ 1699 cm^{-1}. We noted that the peak at ~1732 cm^{-1} in PCBA is attributed to residual PCBM in PCBA. For intrinsic $CsPbI_3$ NCs, OA exists as oleate bound to the NC surface with carboxylate groups, showing asymmetric (υ_{as}(COO) = 1530 cm^{-1}) and symmetric (υ_s(COO) = 1409 cm^{-1}) stretching vibrations. In the $CsPbI_3$ NC-PCBA hybrid, we observed that υ_{PCBA}(C=O) shifts to a lower frequency (by tens of wavenumbers), likely due to coordination or hydrogen bond fracture in solution. The intense peak at 1216 cm^{-1} in the spectrum of $CsPbI_3$-PCBA NCs is assigned to the stretching vibration of C-O (υ_{PCBA}(C-O)). Generally, molecules with carboxylic acid groups coordinate with metallic compounds by splitting C=O and C-O into COO- to form either bidentate chelating or bidentate bridging ring structures

with metal atoms. The presence of υ_{PCBA}(C=O) and υ_{PCBA}(C-O) indicates that a large proportion of PCBA molecules remain as PCBA rather than PCBA ions. Additionally, we observed no υ_{OA}(C=O) signal at 1708 cm^{-1} after the introduction of excessive PCBA, suggesting that the bound oleate molecules have not been significantly replaced by the excessive introduction of PCBA. This discussion applies equally to the $CsPbI_3$ NC-[Bis]PCBA hybrid (Figure S12 (b)).

To verify whether PCBA interacts with $CsPbI_3$ NC surfaces as PCBA-COOH (PCBA in its carboxylic acid form) or PCBA-COO^- (PCBA in its carboxylate form), we further conducted additional FTIR measurements on $CsPbI_3$ NCs with a small amount of fullerene additives. To avoid interference from impurities that could arise from the synthesis of PCBA and [Bis]PCBA and affect the identification of carbonyl (υ(C=O)) and carboxylate ($\upsilon_{as}(COO^-)$ and $\upsilon_s(COO^-)$) stretching vibrations, we used high-purity (>99%) 4-(1',5'-Dihydro-1'-methyl-2'H-[5,6]fullereno-C_{60}-Ih-[1,9-c]-pyrrol-2'-yl)benzoic acid ([SAM]C60) instead of PCBA or [Bis]PCBA. [SAM]C60 has a similar fullerene-derived structure with a carboxyl group, making it a suitable substitute for understanding their interactions with NC. As shown in Figure S12 (c), the FTIR spectra of $CsPbI_3$ NC-[SAM]C60 showed that the characteristic carbonyl stretching peak (υ(C=O)) around 1708 cm^{-1} disappeared. This indicates that the carboxylic acid group converted to a COO^- upon interacting with the NC surface. Given the structural similarity between [SAM]C60 and our compounds, we infer that PCBA and [Bis]PCBA tend to undergo a similar transformation.

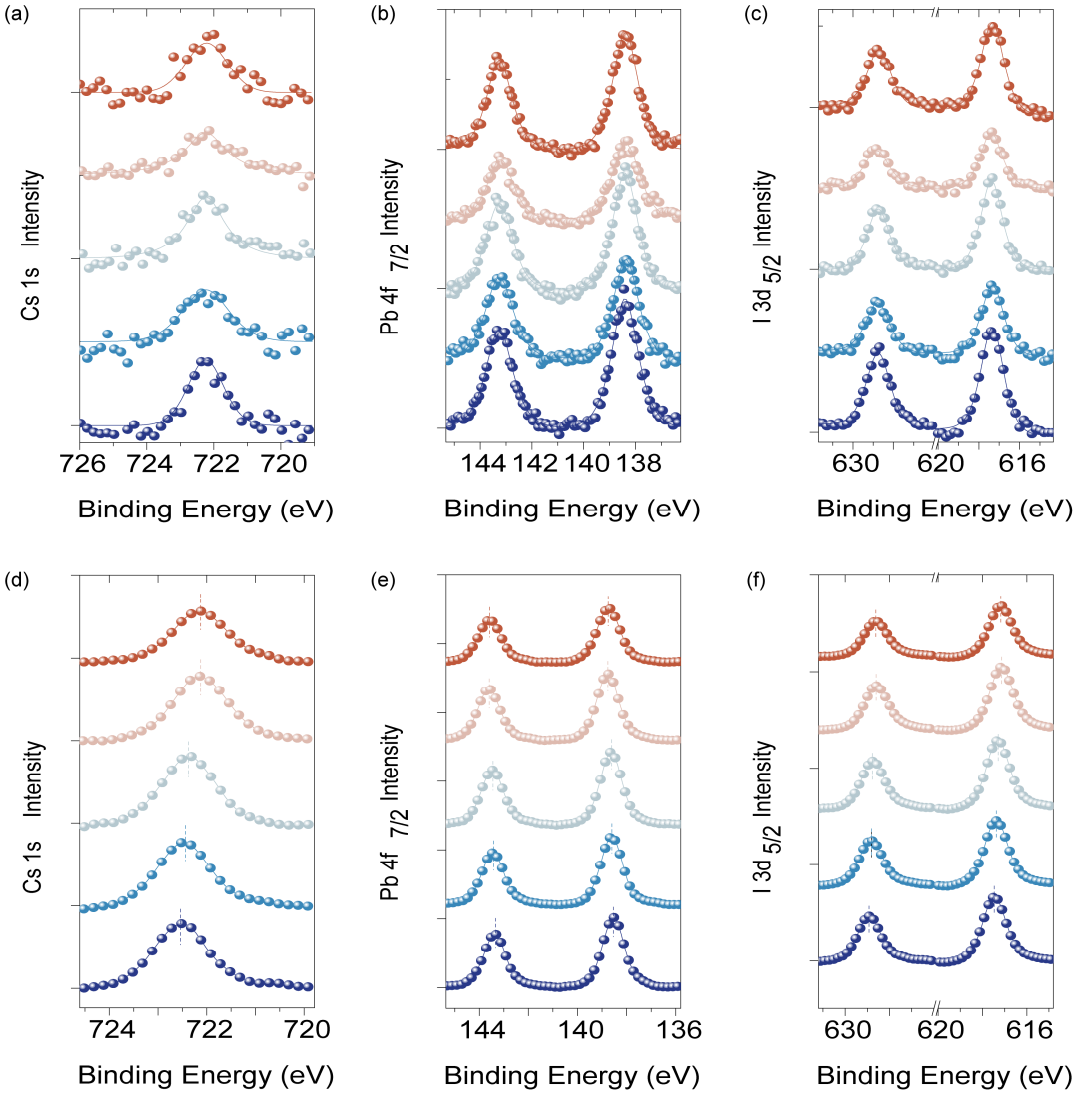

Figure S11. XPS signals of Pb 4f, Cs 1s, and I 3d. Panels (a)-(c) show samples prepared by droplet coating NC solutions, while panels (d)-(f) show samples prepared by spin coating fullerene onto $CsPbI_3$ NC films after removal of alkyl ligands. In each figure, the spectra from bottom to top represent $CsPbI_3$ NC, $CsPbI_3$ NC-PCBM, $CsPbI_3$ NC-[Bis]PCBM, $CsPbI_3$ NC-PCBA, and $CsPbI_3$ NC-[Bis]PCBA, respectively.

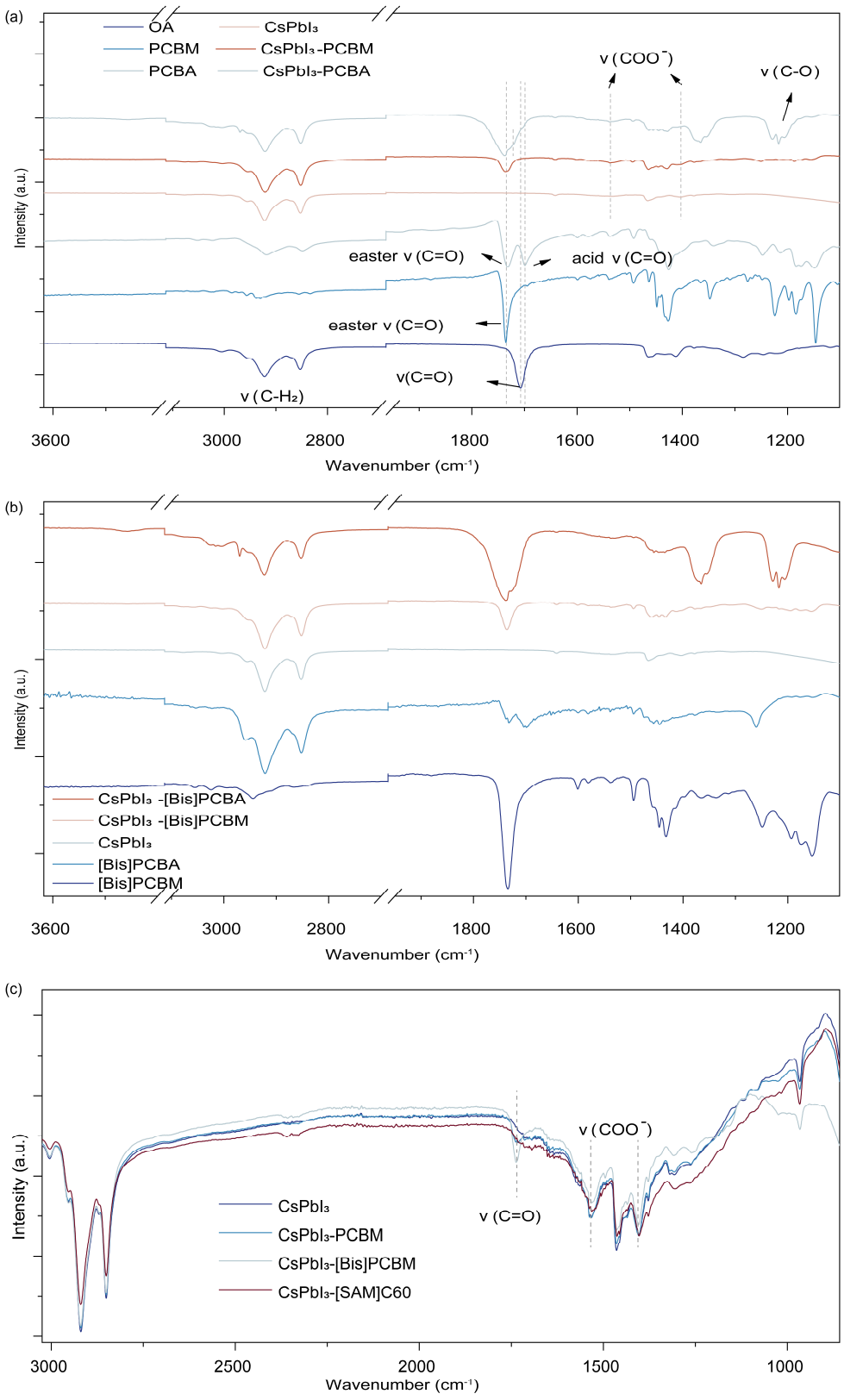

Figure S12 (a) FTIR spectra of $CsPbI_3$ NC, $CsPbI_3$ NC-PCBM, $CsPbI_3$ NC–PCBA, PCBM, PCBA, and OA. (b) FTIR spectra of $CsPbI_3$ NC, $CsPbI_3$ NC-[Bis]PCBM, $CsPbI_3$ NC-[Bis]PCBA, [Bis]PCBM, and [Bis]PCBA. Samples in (a) and (b) were

prepared by adding an excessive amount of fullerene. (c) FTIR spectra of $CsPbI_3$ NC, $CsPbI_3$ NC-PCBM, $CsPbI_3$ NC–[Bis]PCBM, $CsPbI_3$ NC–[SAM]C60. Samples in (c) were prepared with a small amount of fullerene additives.

Supplementary Note 4: Fitting of Energy loss rate

The underlying energy loss mechanisms are determined by the pump fluence and relaxation stage. At low pump fluence, HC relaxation is primarily governed by carrier-phonon interactions. Under the longitudinal optical (LO) phonon interaction mode, the energy loss rate is given by:[2]

$$J_r \approx \frac{3}{2}\frac{\hbar\omega_0}{\tau_{qa}}\left(e^{\frac{\hbar\omega_0}{kT_a}} - e^{\frac{\hbar\omega_0}{kT_p}}\right)\frac{N_q(T_a)}{N_q(T_p)}\left(\frac{kT_p}{\hbar\omega_0}\right)^2 e^{-\frac{\hbar\omega_0}{kT_p}}$$

Where τ_{qa} is the rate constant for LO phonons reaching thermal equilibrium with acoustic phonons, $\hbar\omega_0$ is the phonon energy, T_a is the temperature of acoustic phonons, T_p is the temperature of LO phonons, $N_q(T_p)$ and $N_q(T_a)$ are the LO-phonon occupation numbers at phonon temperatures T_q=T_p and T_q=T_a, respectively. Assuming the HC carrier-LO-phonon system is governed by the decay of LO-phonons into acoustic phonons, the practical energy loss rate can be fitted according to the expression:[3]

$$J_r \approx \frac{3}{2}\frac{\hbar\omega_0}{\tau_{qa}}\left(e^{\frac{\hbar\omega_0}{kT_a}} - e^{\frac{\hbar\omega_0}{kT_c}}\right)\frac{N_q(T_a)}{N_q(T_c)}\left(\frac{kT_c}{\hbar\omega_0}\right)^2 e^{-\frac{\hbar\omega_0}{kT_c}}$$

Where T_c is the carrier temperature. For high pump fluence, HC relation is determined the competition between energy outflow through carrier-phonon interaction and energy inflow due to Auger reheating. In the beginning, carrier-phonon interaction dominated over Auger reheating, thus the energy loss rate can be fitted with the above equation. In Figure 3d, the solid red and blue fitted lines are all based on this LO-phonon emission model.

As the decrease of phonon-related relaxation rate, the HC cooling will be dominated by Auger reheating process, where the energy loss rate is approximately proportional to $(T_c\text{-}T_L)^2$ [4] (T_L is the lattice temperature) . In Figure 3d, the dashed red line is based on this Auger reheating model. We note that the hot phonon bottleneck effect has not been modeled due to its complex nature. However, we believe it plays a role in the

intermediate region between LO-phonon emission and Auger reheating. This analysis is consistent with the discussion in Supplementary Note 5.

Supplementary Note 5: The Three Temperature Model (TTM) and Its Application to Fitting Time-Dependent T_c Profiles

TTM that couples the rate equations of hot carrier and phonons was widely applied to describe hot carrier relaxation and electron-phonon interaction, such as spin-lattice relaxation in manganite oxides,[5] hot electron relaxion in $Bi_2Sr_2CaCu_2O_{8+\delta}$,[6] hot carrier dynamics in graphene[7] and so on. In this work, we adopted the modified TTM developed by M. Monti at el.,[8] which has been successfully used in depicting hot carrier cooling in Sn-Pb mixed perovskite. This model assumes that HCs lose temperature by carrier- longitudinal optical (LO) phonon interaction and give rise to the raising of LO phonon temperature. The HC cooling will be prolonged under high pump fluence by Auger reheating. Meanwhile, LO phonons release its excessive energy by decay into transverse optical phonon or acoustic phonon. According to previous phonon decay mechanism, the temperature of low energy phonon can be replaced with lattice temperature, besides, only one LO phonon branch was adopted here. The coupled rate Equations are shown as following:

$$C_e \frac{dT_c}{dt} = \nabla(k_e \nabla T_c) - G_{ep}(T_c - T_p) + G_A(T_c + T_g)$$

$$C_p \frac{dT_p}{dt} = \nabla(k_e \nabla T_p) + G_{ep}(T_c - T_p) - G_{pp}(T_p - T_L)$$

T_c, $T_{p,i}$, T_L, $C_{e,i}$, $C_{p,i}$, k_e, k_p, $G_{ep,i}$, $G_{pp,i}$ are respectively carrier temperature, phonon temperature, lattice temperature, electron heat capacity, phonon heat capacity, electron heat conductivity, phonon heat conductivity, coupling constant of electron with the phonon branch, coupling constant of phonon branch with the lattice. The term $G_A(T_g+T_c)$ represents Auger heating, where $G_A = k_A N(t)$ and $T_g=2E_g/3k_B$, k_A is Auger recombination rate, $N(t)$ is carrier density, E_g is bandgap. The Time-dependent HC temperature curves

in the main text were numerically fitted with the above equations. By separating the terms in the above two equations, one can distinguish the contributions that slow the HC cooling.

Under lower pump fluence, since the HC energy release mainly occurs through the LO-phonon emission process, the temperature of the LO phonons aligns with the lattice temperature, as shown by the blue dashed lines in Figure 3c. However, under high pump fluence, HC relaxation changes significantly compared with that at low-fluence pump. Specifically, the HC cooling process is not terminated within picosecond but prolonged to tens of picoseconds. In this case, the time dependent temperature can be divided into three stages. Stage (i) is dominated by LO-phonon interaction as same as temperature decay under low pump fluence. It can be demonstrated from the similar value of τ_{LO} (0.47 ps) fitted from the energy power loss rate at this stage. The difference of stage (i) with the temperature decay under low pump fluence lies on HCs eventually heated the LO-phonon to a higher temperature, as the red dash line in Figure 3c. After the LO-phonons attaching to peak temperature, the LO-phonons release energy to acoustic phonon or lattice with a slow rate due to hot phonon bottleneck effect (Stage (ii)). In addition, Auger reheating also contributes the slow HC relaxation in this stage, which can be found in the accelerated temperature decay after removing the Auger reheating effect (orange solid line in Figure 3c). We think stage (iii) is mainly on account of Auger reheating effect since the behavior of energy power loss rate follows quadratic dependence on (T_c-T_L) remarkably well and phonon bottleneck can be neglected due to T_p is close to T_L at this stage. In brief, phonon bottleneck and Auger reheating effects greatly prolong the HC cooling in our $CsPbI_3$ NCs.

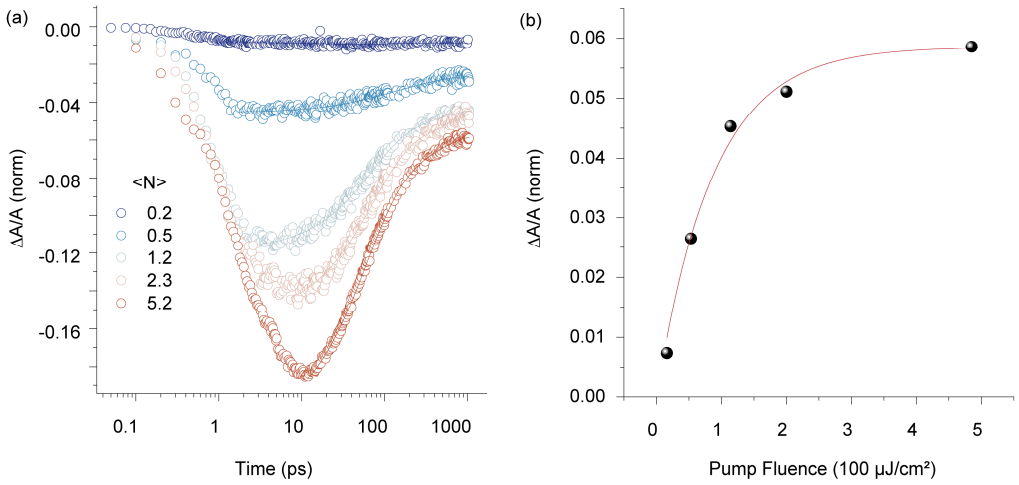

Figure S13. (a) TA kinetics of $CsPbI_3$ NCs probed at 1.88 eV under pump fluence (J) ranging from 16 μJ/cm² to 485 μJ/cm². (b) Intensity of the TA signal in (a) at approximately 1 ns as a function of J. The initial average generated exciton (e-h pair) numbers per NC (<N>) are calculated by fitting the data with $\Delta A/A(J) \propto 1\text{-}\exp(-\langle N \rangle) = 1\text{-}\exp(-J\cdot\sigma)$, where σ is the absorption cross section of the NCs. The average carrier density $n_{0,ave}$ is calculated by $n_{0,\ ave} = \langle N \rangle / d^3$, where d is the average size of the nanocrystals obtained from TEM measurements.

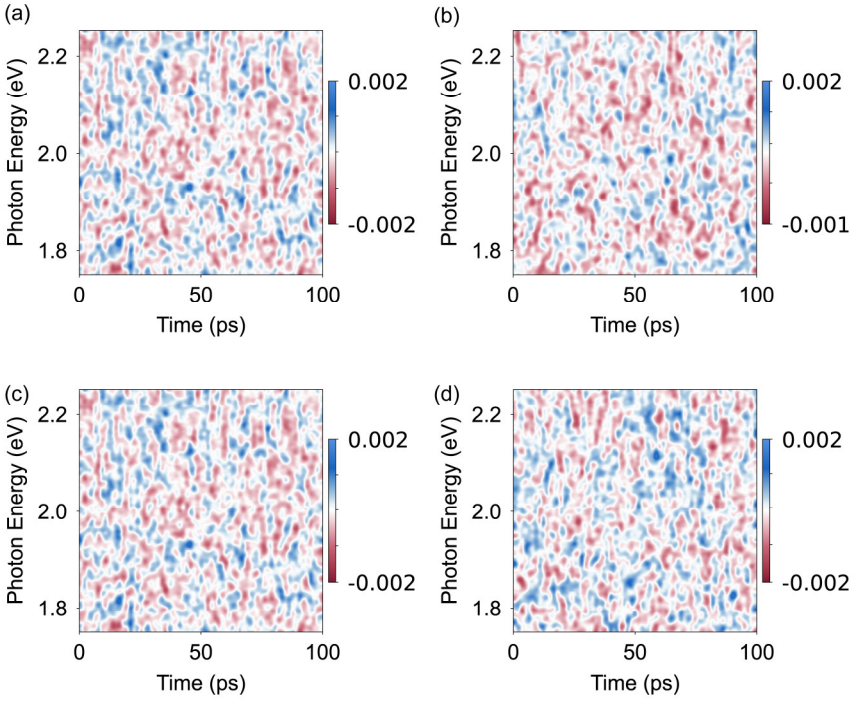

Figure S14. Pseudo color TA maps of (a) PCBM, (b) [Bis]PCBM, (c) PCBA, (d) [Bis]PCBA. The pump fluence is 485 μJ/cm^2.

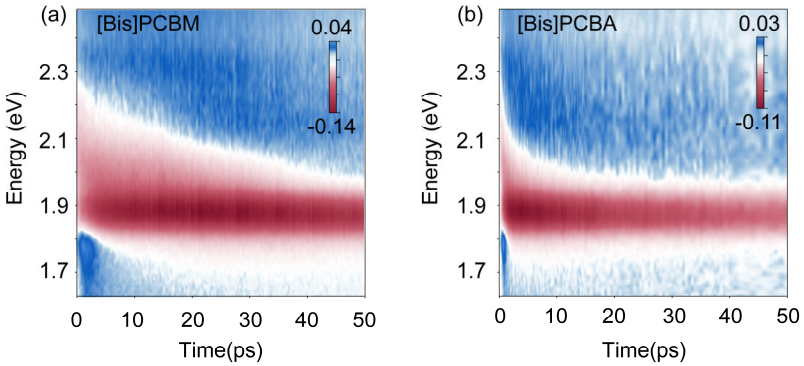

Figure S15. Pseudo color TA maps of (a) $CsPbI_3$ NC-[Bis]PCBM hybrids and (b) $CsPbI_3$ NC-[Bis]PCBM hybrids, excited by a 470 nm pump at $n_{0,\,ave}\approx7.3\times10^{17}$ cm^{-3}.

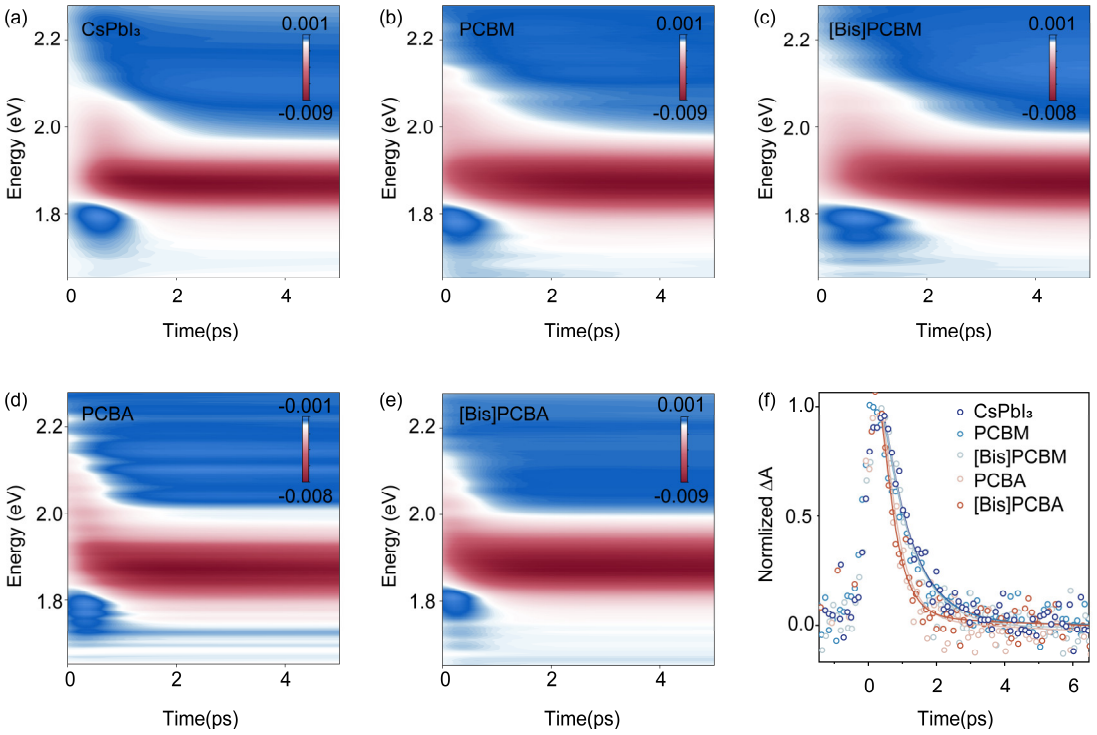

Figure S16. Pseudo color TA maps of (a) $CsPbI_3$ NC, (b) $CsPbI_3$ NC-PCBM hybrids, (c) $CsPbI_3$ NC-[Bis]PCBM hybrids, (d) $CsPbI_3$ NC-PCBA hybrids, and (e) $CsPbI_3$ NC-[Bis]PCBA hybrids, excited by a 470 nm pump at $n_{0,\,ave}\approx6.6\times10^{16}$ cm^{-3}. The presented pseudo-color TA maps have been denoised using global fitting, which does not affect the overall trends observed. (f) IBP kinetics of (a-e). The calculated capture efficiency (η) for PCBA and [Bis]PCBA are 29% and 30%, respectively.

Table S3. Averaged decay constants (τ) of the HCs fitted from the kinetic curves at the isosbestic point (IBP) on the higher energy side of the ground state PB signal

	τ ($n_{0,\ ave}$≈7.3×10^{17} cm^{-3}) (ps)	τ ($n_{0,\ ave}$≈6.6×10^{16} cm^{-3}) (ps)
$CsPbI_3$ NCs	22.65	0.86
$CsPbI_3$ NCs-PCBM	20.32	0.82
$CsPbI_3$ NCs-[Bis]PCBM	22.50	0.79
$CsPbI_3$ NCs-PCBA	7.69	0.61
$CsPbI_3$ NCs-[Bis]PCBA	5.48	0.60

References

[1] M. Saba, M. Cadelano, D. Marongiu, F. Chen, V. Sarritzu, N. Sestu, C. Figus, M. Aresti, R. Piras, A. G. Lehmann, C. Cannas, A. Musinu, F. Quochi, A. Mura, G. Bongiovanni, *Nat. Commun.* **2014**, 5, 5049.

[2] V. V. Klimov, P. Haring Bolivar, H. Kurz, *Phys. Rev. B Condens. Matter* **1995**, 52, 4728.

[3] M. Li, S. Bhaumik, T. W. Goh, M. S. Kumar, N. Yantara, M. Gratzel, S. Mhaisalkar, N. Mathews, T. C. Sum, *Nat. Commun.* **2017**, 8, 14350.

[4] M. Achermann, A. P. Bartko, J. A. Hollingsworth, V. I. Klimov, *Nat. Phys.* **2006**, 2, 557.

[5] R. D. Averitt, A. J. Taylor, *J. Phys. Condens. Matter* **2002**, 14, R1357.

[6] L. Perfetti, P. A. Loukakos, M. Lisowski, U. Bovensiepen, H. Eisaki, M. Wolf, *Phys. Rev. Lett.* **2007**, 99, 197001.

[7] J. C. Johannsen, S. Ulstrup, F. Cilento, A. Crepaldi, M. Zacchigna, C. Cacho, I. C. E. Turcu, E. Springate, F. Fromm, C. Raidel, T. Seyller, F. Parmigiani, M. Grioni, P. Hofmann, *Phys. Rev. Lett.* **2013**, 111, 027403.

[8] A. P. Kirk, M. V. Fischetti, *Phys. Rev. B* **2012**, 86.